The 8th European Congress on Computational Methods in Applied Sciences and Engineering
ECCOMAS Congress 2022
5-–9 June 2022, Oslo, Norway

HEMODYNAMICS IN HEALTHY AND PATHOLOGICAL THORACIC AORTA: INTEGRATION OF *IN-VIVO* DATA IN CFD SIMULATIONS AND IN *IN-VITRO* EXPERIMENTS

Alessandro Mariotti[1], Emanuele Vignali[2], Emanuele Gasparotti[2], Pietro Marchese[3,4], Mario Morello[1], Maria Vittoria Salvetti[1], and Simona Celi[2]

[1] Dipartimento di Ingegneria Civile ed Industriale, University of Pisa, Pisa, Italy
Largo Lucio Lazzarino 2, 56122 Pisa, Italia
e-mail: alessandro.mariotti@unipi.it, m.morello1@studenti.unipi.it, mv.salvetti@ing.unipi.it

[2] BioCardioLab - Heart Hospital, Fondazione Toscana G. Monasterio, Massa, Italy
Via Aurelia Sud, 54100 Massa, Italia
email: evignali@ftgm.it, emanuele.gasparotti@ftgm.it, s.celi@ftgm.it

[3] Institute of Life Sciences, Scuola Superiore Sant'Anna, Pisa, Italy
Piazza Martiri della Libertà, 33, 56127 Pisa, Italia
email: pietro.marchese@santannapisa.it

[4] Fondazione Toscana G. Monasterio, Massa, Italy
Via Aurelia Sud, 54100 Massa, Italia

Key words: Hemodynamics, CFD simulations, thoracic aorta, *in-vivo* data, CFD vs. *in-vitro* experiments

Abstract. A comparison between the results of the CFD simulations and the *in-vitro* experiments carried out on a circulatory mock loop is presented. Both approaches integrate *in-vivo* measurements obtained from a patient-specific clinical data set. Three thoracic-aorta geometries are analyzed: a healthy aorta, an aneurysmatic aorta, and a coarctated aorta. The healthy geometry is obtained from Magnetic Resonance Imaging (MRI) acquisitions, together with the patient-specific flow-rate waveform, whereas the diseased ones are derived from the former geometry by locally morphing the vessel's wall. The open-source code Simvascular is used for simulations. The *in-vitro* results are measured in a fully controlled and sensorized circulatory mock loop for 3D-printed aortic models. Differently from *in-vivo* acquisitions, the experimental set-up eliminates some of the uncontrollable uncertainties that characterize MRI data. Indeed, perfect control of the flow rate and full knowledge of the wall model characteristics (rigid walls in the present case) is allowed in experiments and, thus, clear indications can be obtained to validate and improve the accuracy of numerical models. The numerical and experimental results are in good agreements for the three analyzed geometries and the flow-rate conditions. *In-vivo* data from the healthy case are in a satisfactory agreement with numerical/*in-vitro* results, and they can be ascribed to possible differences between MRI and numerical/*in-vitro* set-ups. The velocity fields obtained through CFD are consistent with the echographic results in *in-vitro* experiments, showing the same flow patterns in healthy and pathological cases.

1 INTRODUCTION

Congenital Heart Diseases (CHD) are structural abnormalities of the heart or of the large vessels. The emergence and development of these diseases can be related to hemodynamic forces and anomalies. In the last years, the merging of patient-specific multimodal imaging (such as Phase-Contrast Magnetic Resonance Imaging, PC-MRI) and Computational Fluid Dynamics (CFD) simulations has been used to provide clinical information at a patient-specific level. CFD simulations evaluate the distribution of hemodynamic quantities of interest guaranteeing time and spatial resolutions that cannot be obtained from any clinical approach. They also compute additional flow descriptors, such as wall shear stresses, which can not be quantified by any *in-vivo* measurements. On the other hand, different sources of uncertainties are present in CFD models, which may affect the accuracy of the evaluation of the output quantities of interest. Among them, there is the imposition of appropriate and accurate boundary conditions [1–8]. To overcome this drawback, it is possible to use non-invasive *in-vivo* measurement [9–11] as boundary conditions for simulations [12–16], as well as validation sources for numerical results. Indeed, these clinical data have been used, together with CFD, to study the hemodynamic behavior of healthy [12–14, 16, 17] and diseased [3, 6, 7, 18–21] patients. However, from the comparison between *in-vivo* MRI data and simulation results, some differences are often present, especially in terms of velocity distribution and of time delay (see, e.g., [16]). These differences are probably related to some features of the *in-vivo* data that are difficult to be completely characterized and/or controlled, such as the vessel-wall properties and the position of the vessel during the cardiac cycle. To eliminate, or at least reduce, many of these uncertainties, a fully-controlled and sensorized circulatory mock loop for 3D-printed aortic models has been proposed in [22]. This experimental set-up guarantees a perfect control of the flow rate, pressure conditions and the possibility to explore patient specific morphologies with known wall-model features. In this way, clearer indications can be obtained to assess and possibly improve the accuracy of CFD models (vs. *in-vitro* data) and to single out the importance of the differences between *in-vivo* and *in-vitro* set-ups.

A comparison between CFD results and *in-vitro* measurements is presented herein. Both approaches see the integration of *in-vivo* data obtained from a patient-specific clinical dataset. Three thoracic aorta geometries are taken into account: a healthy aorta, an aneurysmal aorta, and a coarctated aorta. The former comes from a clinical dataset [16], whereas the diseased ones are derived from the former geometry and obtained with virtual shape modifications. The open-source code Simvascular is used to carry out the numerical simulations. *In-vitro* data are obtained from the circulatory mock loop for 3D-printed aortic models developed in [22]. Results are compared in terms of flow-rate waveforms at the descending aorta outlet section, differential pressure between the ascending and the descending aorta, and velocity fields in different portions of the aorta obtained through echography in experiments. Finally, instantaneous-flow streamlines, Wall Shear Stresses (WSS), and Time-Averaged Wall Shear Stresses (TAWSS) are investigated for the three geometries.

2 PROBLEM DEFINITION, NUMERICAL AND EXPERIMENTAL SET-UPS

The study is based on the clinical dataset in [16]: the patient is a 28-years-old male with a tricuspid aortic valve. The dataset includes MRI acquisitions obtained by means of the Philips

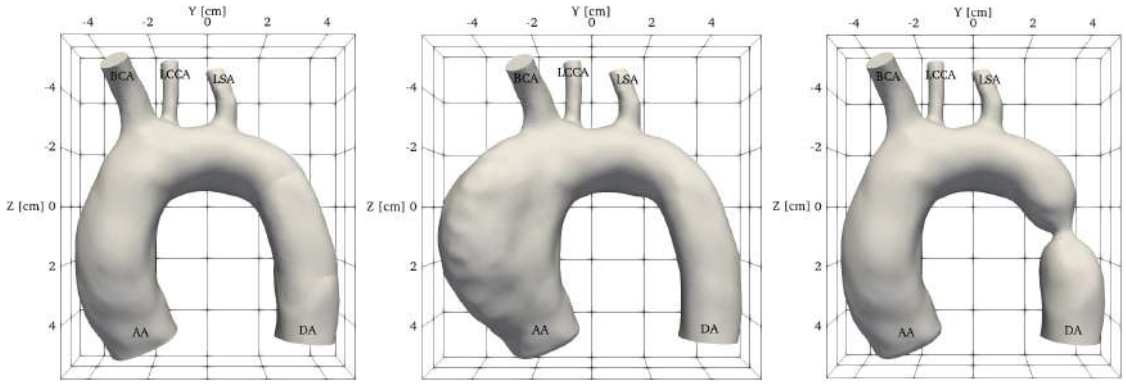

(a) (b) (c)

Figure 1: Sketches of the investigated geometries: (a) healthy aorta, (b) aortic aneurysm, and (c) coarctated aorta.

Ingenia 3T MRI Scanner. Starting from the segmentation of the 3D whole-heart MRI images, the model of the healthy thoracic aorta is reconstructed (Fig. 1(a)). From this geometry, two additional geometries are obtained by locally morphing the lateral walls of the vessel. In particular, the surface modifications were obtained by using a CAD software under the supervision of a skilled clinician in order to reproduce realistic pathological conditions. The two additional geometries reproduce examples of an aneurysm and a coarctation of the aorta. The aneurysm is located in the ascending aorta, whereas the coarctation occurs in the descending one, as shown in Fig. 1(b) and Fig. 1(c), respectively. The patient's dataset includes the flow rate in the ascending aorta obtained by means of Phase Contrast Magnetic Resonance Imaging (PC-MRI). The MRI dataset volume is retrospectively reconstructed with the Phase-Contrast Magnetic Resonance Angiography (PC-MRA) technique (further details are provided in [16]).

Blood is modeled herein as a Newtonian and incompressible fluid, as widely accepted in large vessels, with density and kinematic viscosity equal to $\rho = 1.06\,\mathrm{g\,cm^{-3}}$ and $\nu = 3.77 \times 10^{-2}\,\mathrm{cm^2\,s^{-1}}$. The three-dimensional Navier-Stokes equations for incompressible flows are considered as governing equations. A no-slip condition was imposed between the fluid and the walls, which were assumed rigid for all simulations since the experimental model is rigid. At the inlet of the computational domain, a Dirichlet-type boundary condition is used with a uniform velocity in

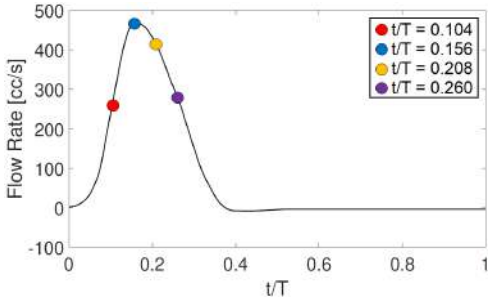

Figure 2: Inlet flow-rate waveform.

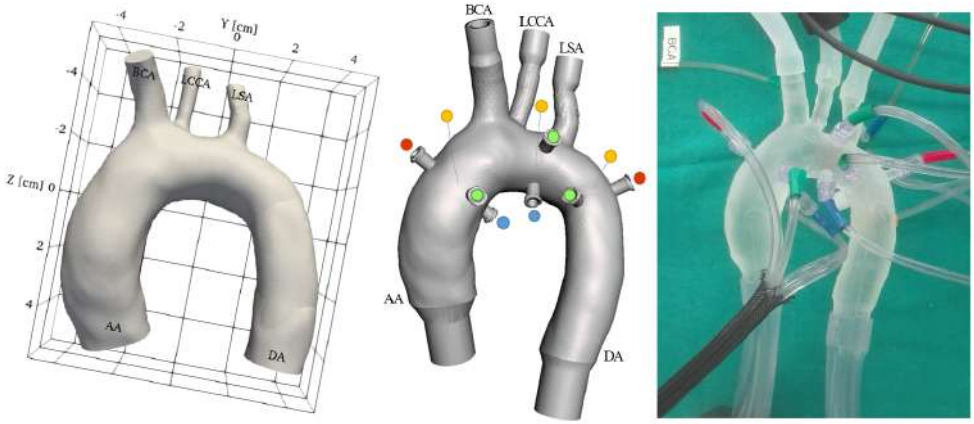

(a) (b) (c)

Figure 3: (a) Patient-specific geometry, (b) geometry for 3D printing including pressure taps, and (c) 3D-printed geometry for the circulatory mock loop.

space, i.e. plug flow, with the MRI-measured flow-rate waveform. At the outflows, a Neumann condition on pressure is specified, based on the 3-element Windkessel model [25]. We perform the simulations by using the open-source software SimVascular [23]. A finite-element approach including SUPG/PSPG stabilizing terms is used to carry out the numerical simulations; P1-P1 elements, i.e. linear shape functions for both velocity and pressure, are chosen. Additional stabilizing terms are introduced to prevent also the numerical instabilities due to backflow at the outlets [24].

For the *in-vitro* experiments, the set-up described in [22] is used. The active component of the circulatory mock loop is given by a custom speed-controlled piston pump. The patient-specific flow-rate waveform, shown in Fig. 2, is used to configure the pump-speed profile, after an automatic interpolation process of that waveform. 3D rigid models for each of the three thoracic aortas are printed in laser stereolithography (see Fig. 3). The resistive and capacitive components of the three-element Windkessel models are introduced in the circulatory mock loop with pinch valves and air-filled rigid chambers, respectively. Flow and pressure waveforms are obtained through dedicated clamp-on ultrasound flowmeters (Sonotec) and color-coded plugin catheter probes (TruWave transducers) connected at the different section levels. The pump actuation and the sensor acquisition are managed with a real-time PLC processor. Velocity-field distributions are acquired through echography by means of Vortex Flow Analysis and color Doppler acquisition procedures. All the experiments are conducted using a mixture of water and glycerol (in the volume proportion of 60% and 40%, respectively) as working fluid. In this way, it is possible to reproduce the density ($1.06\,\mathrm{g\,cm^{-3}}$) and the viscosity ($3.6 \times 10^{-3}\,\mathrm{Pa\,s}$) of the blood.

3 RESULTS AND DISCUSSION

Figure 4(a) shows the flow-rate waveforms at the descending aorta obtained in *in-vitro* experiments and simulations for the three investigated geometries. For the healthy aorta, *in-vivo* MRI data is also reported for comparison. The agreement between experiments and simula-

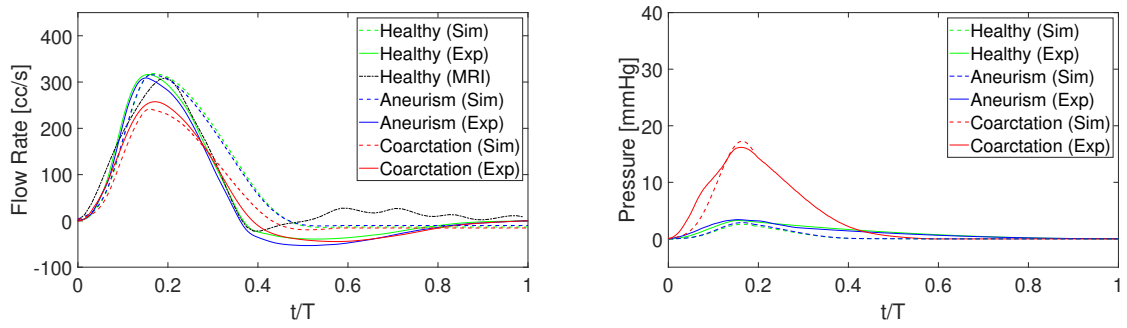

(a) (b)

Figure 4: (a) Flow-rate waveforms at the descending aorta: *in-vivo*, *in-vitro* and CFD results. (b) Differential pressure between the ascending and the descending aorta: *in-vitro* and CFD results.

tions is good, with acceptable errors at systolic peaks. *In-vitro* and numerical flow-rate peaks in the descending aorta are in perfect agreement in time. *In-vivo* data matches simulations and experiments from the healthy case. Discrepancies can be ascribed to possible differences between MRI data and numerical/*in-vitro* set-ups. The time difference at the systolic peak between simulated/*in-vitro* waveforms and MRI data is probably related to the effect of the wall compliance of the real aorta, as previously inferred in [16].

Excellent agreement in terms of differential pressure curves is found between CFD and *in-vitro* results for all the considered healthy and pathological aortas (see Fig. 4(b)). As expected, the highest differential pressure ascending/descending aorta is found at the systolic peak for the coarctation and it is related with the presence of the restricted section. This behavior is in line with the actual pathological condition in terms of pressure.

Figures 5 and 6 compare the instantaneous-flow streamlines in CFD simulations with the echographic results from the *in-vitro* experiments. Three different time instants during the cardiac cycle are shown, viz. t/T= 0.156, t/T= 0.208, and t/T= 0.260, which are also highlighted with circles in Fig. 2. The streamlines are evaluated in the same measurement region of the echography and they are colored according to the velocity magnitude. The investigations are carried out for the ascending aorta in the aneurismatic geometry (Fig. 5) and for the descending aorta in the coarctation (Fig. 6). Both of them are compared with the healthy subject. The velocity fields obtained through CFD are in a good agreement with the echography results in *in-vitro* experiments in terms of streamline patterns and distribution. The comparison between the echographic acquisitions and the CFD data allows us to analyze the differences in flow topology between the healthy and pathological cases. Flow recirculations are absent in the healthy geometry at the systolic peak (t/T= 0.156 in Figs. 5 and 6), while they are evident in the aneurismatic region and along the aortic arch for the coarctation. Highly distorted flow and recirculations are also present in the aneurismatic region and in the aortic arch upstream of the coarctation at the early diastole (t/T= 0.208 in Figs. 5 and 6, respectively). Blood recirculations and distorted flow in the ascending aorta are present in all the three geometries during the diastole (t/T= 0.260 in Figs. 5 and 6). For the coarctation, large distortion and recirculations can be seen also in the aortic arch upstream of the coarctation, as in the previous time instants.

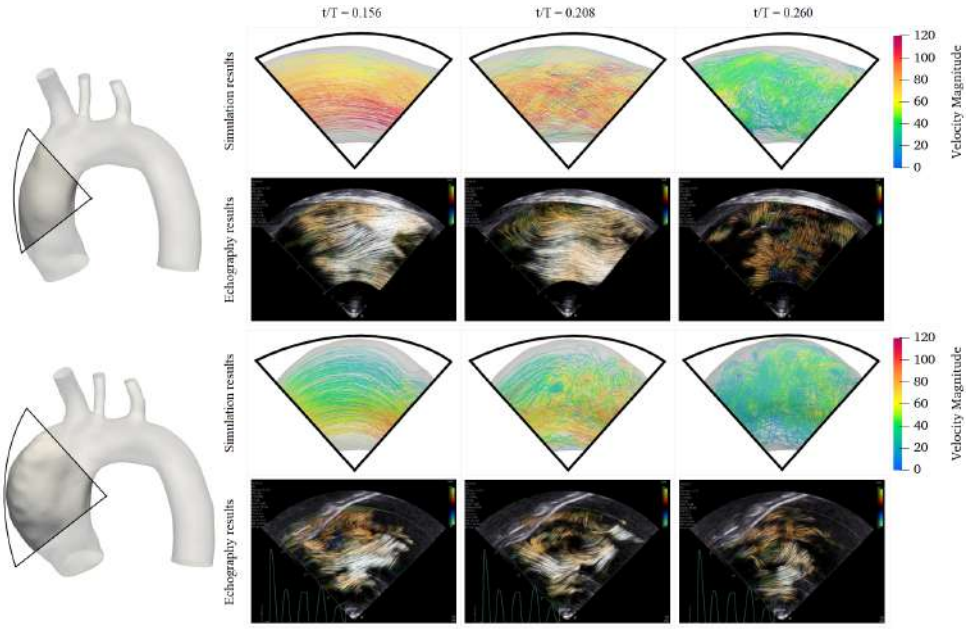

Figure 5: Comparison between the instantaneous flow streamlines colored according to the velocity magnitude and the echographic results for three time instants during the cardiac cycle: healthy and aneurismatic aortas.

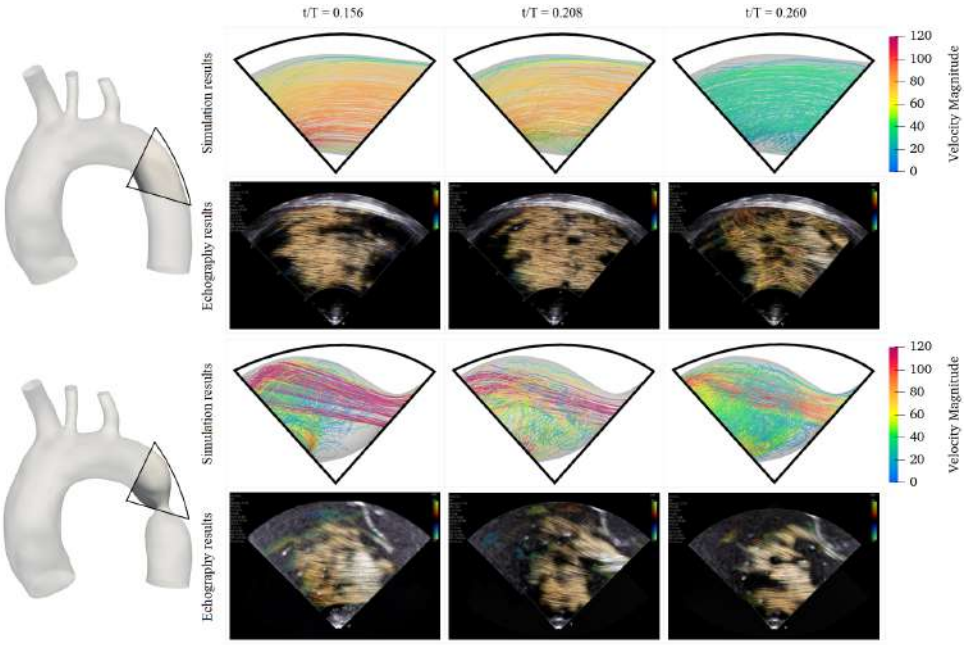

Figure 6: Comparison between the instantaneous flow streamlines colored according to the velocity magnitude and the echographic results for three time instants during the cardiac cycle: healthy and coarctated aortas.

The analysis of the 3D instantaneous flow streamlines and of the wall shear stresses are reported in Figs. 7−10. Four different time instants during the cardiac cycle are considered, viz. t/T= 0.104, t/T= 0.156, t/T= 0.208, and t/T= 0.260. Instantaneous Wall Shear Stresses (WSS) and Time-Averaged Wall Shear Stresses (TAWSS) are shown. As mentioned before, stresses are very important hemodynamic descriptors since they play a fundamental role in the formation and growth of vascular diseases, and they cannot be quantified in any *in-vivo* measurements with a satisfactory level of accuracy. WSS is defined as the modulus of the tangential stress $\vec{\tau}$ exerted by the flow on the arterial wall, that is:

$$\mathrm{WSS}\,(\vec{x},t) = |\vec{\tau}\,(\vec{x},t)| \tag{1}$$

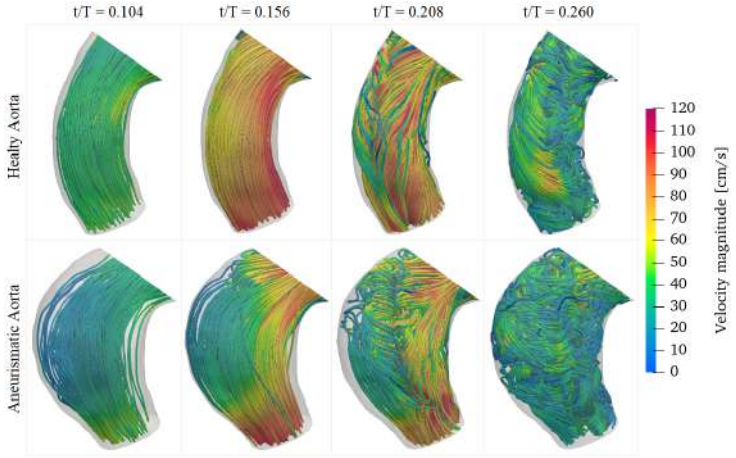

Figure 7: Instantaneous-flow streamlines colored according to the velocity magnitude: ascending aorta for healthy and aneurismatic cases.

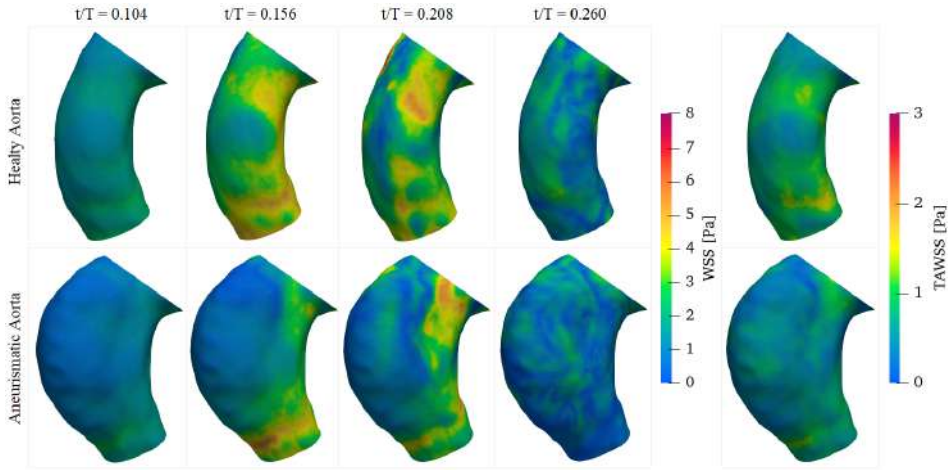

Figure 8: Instantaneous WSS and TAWSS distributions: ascending aorta for healthy and aneurismatic cases.

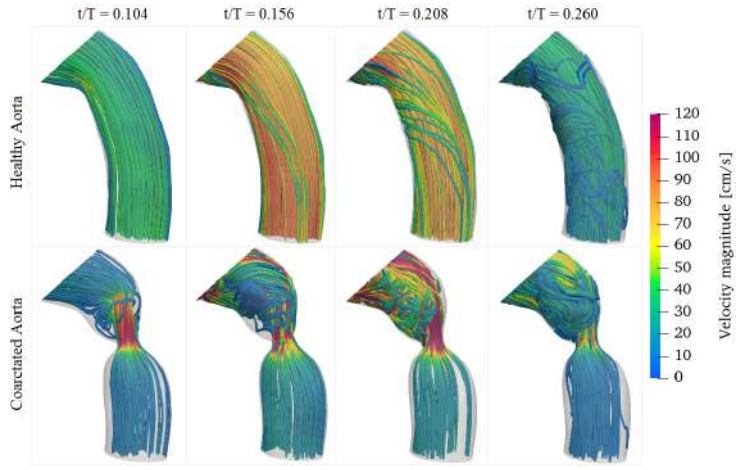

Figure 9: Instantaneous-flow streamlines colored according to the velocity magnitude: descending aorta for healthy and coarctated cases.

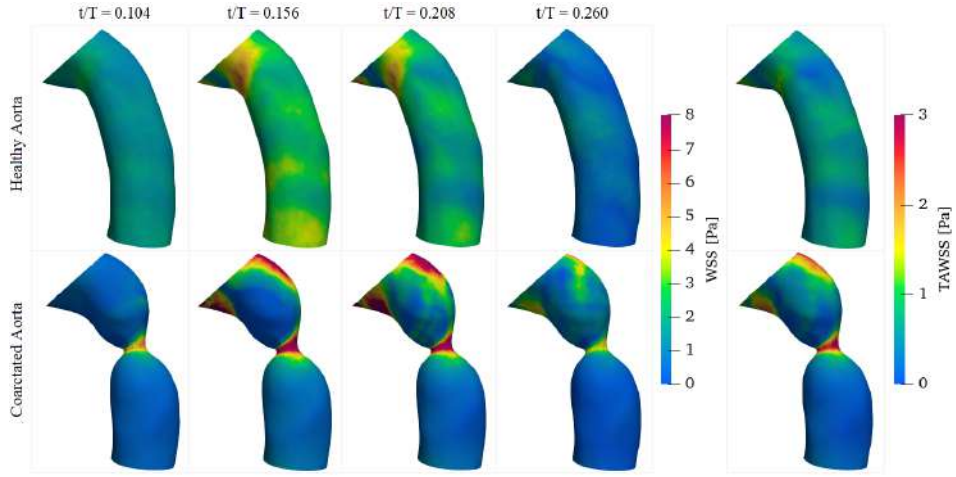

Figure 10: Instantaneous WSS and TAWSS distributions: descending aorta for healthy and coarctated cases.

TAWSS is obtained averaging instantaneous wall shear stresses during the whole cardiac cycle, as follows:

$$\mathrm{TAWSS}\left(\vec{x}\right) = \frac{1}{\mathrm{T}} \int_0^{\mathrm{T}} \left|\vec{\tau}\left(\vec{x}, t\right)\right| \, \mathrm{d}t \tag{2}$$

where T is the time-length of a cardiac cycle.

The comparisons between the healthy and the pathological aortas are carried out for the ascending aorta in the case of aneurysm (Figs. 7 and 8) and the descending aorta for the coarctation (Figs. 9 and 10). Regions with low velocities and localized recirculations are present in the aneurysmatic subject rather than in the healthy aorta (Fig. 7), which lead to lower values of stresses, both instantaneous and cycle-averaged (Fig. 8). On the other hand, a considerable in-

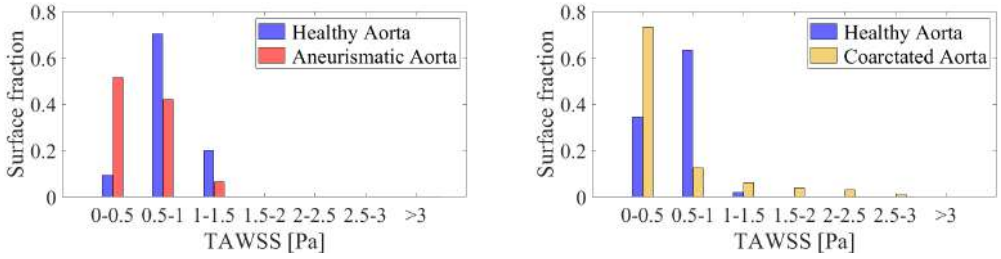

Figure 11: Surface fraction of the TAWSS: (a) ascending aorta for healthy and aneurismatic cases, (b) descending aorta for healthy and coarctated aorta.

crease in the velocity magnitude near the restricted section of the coarctation is found compared to healthy geometry (Fig. 9). Furthermore, the sudden variation of the vessel geometry leads to the generation of two significant recirculation regions, i.e. one upstream and the other downstream of the coarctation site. This results in very high values of the wall shear stress around the narrower section (Fig. 10). On the contrary, WSS and TAWSS are low in the flow-recirculation areas.

To better quantify and compare the TAWSS distributions, we define 7 stress levels, equally distributed, from level 1, defined as $0\,\text{Pa} \leq \text{TAWSS} < 0.5\,\text{Pa}$, to level 7, defined as $\text{TAWSS} > 3\,\text{Pa}$: all the intervals are equally-spaced at 0.5 Pa. The surface fractions associated with the different stress levels are shown in Fig. 11. The aneurismatic aorta is characterized by lower stresses than the healthy geometry, whereas the coarctation presents both higher and lower values of TAWSS.

4 CONCLUSION

In this study, a comparison between the experimental results and those obtained through the hemodynamic simulation was performed. Both approaches integrate *in-vivo* measurements from a patient-specific clinical dataset. The open-source code Simvascular is used for numerical simulations. *In-vitro* data are obtained by a fully controlled and sensorized circulatory mock loop for 3D-printed aortic models. Three thoracic aorta geometries are analyzed: a healthy aorta, an aneurysmatic aorta, and a coarctated aorta. The CFD and *in-vitro* results are mutually consistent. *In-vivo* data from the healthy case are in a satisfactory agreement with numerical/*in-vitro* results, and they can be ascribed to possible differences between MRI and numerical/*in-vitro* set-ups. Numerical results are compared with the echography results in *in-vitro* experiments and the 3D distributions of the streamlines and the wall shear stresses have been investigated. Low-velocity regions and local recirculations are present in the aneurysm region, resulting in lower values of stresses. Regarding the coarctated aorta, there is a considerable increase in the velocity magnitude near the restricted section, compared to healthy geometry, and this results in very high stresses in the narrowed section.

REFERENCES

[1] Schiavazzi, D.E., Arbia, G., Baker, C. Hlavacek, A.M., Hsia, T.Y., Marsden, A.L., and Vignon-Clementel, I.E. Uncertainty quantification in virtual surgery hemodynamics predictions for single ventricle palliation. International Journal for Numerical Methods in Biomedical Engineering, 32(3):1-25, 2016.

[2] Sarrami-Foroushani, A., Lassila, T., Gooya, A., Geers, A.J. and Frangi, A.F. Uncertainty quantification of wall shear stress in intracranial aneurysms using a data-driven statistical model of systemic blood flow variability. Journal of biomechanics, 49:3815-3823, 2016.

[3] Boccadifuoco, A., Mariotti, A., Celi, S., Martini, N., and Salvetti, M.V., Uncertainty quantification in numerical simulations of the flow in thoracic aortic aneurysms, Proceedings of the 7th European Congress on Computational Methods in Applied Sciences and Engineering (ECCOMAS Congress 2016), **3**, 6226-6249, (2016).

[4] Brault, A., Dumas, L., and Lucor, D. Uncertainty quantification of inflow boundary condition and proximal arterial stiffness-coupled effect on pulse wave propagation in a vascular network. International Journal for Numerical Methods in Biomedical Engineering, 33(10) 2017.

[5] Bozzi, S., Morbiducci, U., Gallo, D., Ponzini, R., Rizzo, G., Bignardi, C. and Passoni, G.. Uncertainty propagation of phase contrast-MRI derived inlet boundary conditions in computational hemodynamics models of thoracic aorta. *Computer Methods in Biomechanics and Biomedical Engineering* (2017) **20**(10):1104-1112.

[6] Boccadifuoco, A., Mariotti, A., Celi, S., Martini, N. and Salvetti, M.V.: Impact of uncertainties in outflow boundary conditions on the predictions of hemodynamic simulations of ascending thoracic aortic aneurysms, Comput. Fluids, **1**65, 96-115, (2018).

[7] Antonuccio, M.N., Mariotti, A., Fanni, B.M., Capellini, K., Capelli, C., Sauvage, E., and Celi, S. Effects of Uncertainty of Outlet Boundary Conditions in a Patient-Specific Case of Aortic Coarctation Ann. Biomed. Eng., **4**9(12), 3494–3507 (2021)

[8] Mariotti, A., Boccadifuoco, A., Celi, S., and Salvetti, M.V. Hemodynamics and stresses in numerical simulations of the thoracic aorta: Stochastic sensitivity analysis to inlet flow-rate waveform, Comput. Fluids, **230**, 105123, (2021)

[9] Efstathopoulos, E.P. and Patatoukas, G. and Pantos, I. and Benekos, O. and Katritsis, D. and Kelekis, N.L.: Wall shear stress calculation in ascending aorta using phase contrast magnetic resonance imaging. Investigating effective ways to calculate it in clinical practice, Physica Medica, **24(4)**, 175–181, (2008).

[10] Markl, M., Wallis, W. and Harlo, A. Reproducibility of flow and wall shear stress analysis using flow-sensitive four-dimensional MRI. Journal of Magnetic Resonance Imaging, **33(4)**, 988-994, (2011).

[11] Morbiducci, U., Ponzini, R., Rizzo, G. Cadioli, M., Esposito, A., Montevecchi, F.M., and Redaelli, A. Mechanistic insight into the physiological relevance of helical blood flow in the human aorta: An in vivo study. Biomechanics and Modeling in Mechanobiology, **10(3)**, 339-355, (2011).

[12] Gallo, D., De Santis, G., Negri, F., Tresoldi, D., Ponzini, R., Massai, D., Deriu, M.A., Segers, P., Verhegghe, B., Rizzo, G., and Morbiducci, U. On the use of in vivo measured flow rates as boundary conditions for image-based hemodynamic models of the human aorta: implications for indicators of abnormal flow, Ann. Biomed. Eng., **40**(3):729-741, (2012).

[13] Morbiducci, U., Ponzini, R., Gallo, D., Bignardi, C., and Rizzo, G.: Inflow boundary conditions for image-based computational hemodynamics: Impact of idealized versus measured velocity profiles in the human aorta, J. Biomech., **46(1)**, 102-109, (2013).

[14] Morbiducci, U., Gallo, D., Cristofanelli, S., Ponzini, R., Deriu, M.A., Rizzo, G., and Steinman, D.A. A rational approach to defining principal axes of multidirectional wall shear stress in realistic vascular geometries, with application to the study of the influence of helical flow on wall shear stress directionality in aorta, J. Biomech., **48(6)**, 899, (2015).

[15] Condemi, F., Campisi, S., Viallon, M., Troalen, T., Xuexin, G., Barker, A.J., Markl, M., Croisille, P., Trabelsi, O., Cavinato, C., Duprey, and A. Avril, S.: Fluid- and biomechanical analysis of ascending thoracic aorta aneurysm with concomitant aortic insufficiency, Ann. Biomed. Eng., **45(12)**, 2921, (2017).

[16] Boccadifuoco, A., Mariotti, A. Capellini, K., Celi, S. and Salvetti, M.V. Validation of numerical simulations of thoracic aorta hemodynamics: comparison with *in-vivo* measurements and stochastic sensitivity analysis. Cardiovascular Engineering and Technology, **4**:688-706, (2018)

[17] Youssefi, P. and Gomez, A. and Arthurs, C. and Sharma, R. and Jahangiri, M. and Figueroa, C.A.: Impact of patient-specific inflow velocity profile on hemodynamics of the thoracic aorta, J. Biomech. Eng., **140(1)**, 1011002, (2018).

[18] Campbell, I.C. and Ries, J. and Dhawan, S.S. and Quyyumi, A.A. and Taylor, W.R. and Oshinski, J.N.: Effect of inlet velocity profiles on patient-specific computational fluid dynamics simulations of the carotid bifurcation, J. Biomech. Eng., **134(5)**, 051001, (2012).

[19] Chandra, S., Raut, S. S., Jana, A., Biederman, R. W., Doyle, M., Muluk, S. C., Finol, E. A.: Fluid-Structure Interaction Modeling of Abdominal Aortic Aneurysms: The Impact of Patient-Specific Inflow Conditions and Fluid/Solid Coupling, ASME J. Biomech. Eng., **135(8)**, 081001, (2013)

[20] Pasta, S., Rinaudo, A., Luca, A., Pilato, M., Scardulla, C., Gleason, T.G., and Vorp, D.A.: Difference in hemodynamic and wall stress of ascending thoracic aortic aneurysms with bicuspid and tricuspid aortic valve. J. Biomech., **46(10)**, 1729, (2013).

[21] Capellini, K., Vignali, E., Costa, E., et al.: Computational fluid dynamic study for ATAA hemodynamics: an integrated image-based and radial basis functions mesh morphing approach, J. Biomech. Eng, **1**40(11), 111007 (2018).

[22] Vignali, E., Gasparotti, E., Mariotti, A., Haxhiademi, D., Ait-Ali, L., and Celi, S.: High-Versatility Left Ventricle Pump and Aortic Mock Circulatory Loop Development for Patient-Specific Hemodynamic In Vitro Analysis, ASAIO Journal, doi: 10.1097/MAT.0000000000001651, (2022).

[23] Updegrove, A., Wilson, N.M., Merkow, J., Lan, H., Marsden, A.L., and Shadden S.C.: Simvascular: An open source pipeline for cardiovascular simulation. Ann. Biomed. Eng., **45(3)**, 525–541, (2016) .

[24] Esmaily Moghadam, M., Bazilevs, Y., Hsia, T. Y., Vignon-Clementel, I. E., and Marsden, A. L.: A comparison of outlet boundary treatments for prevention of backflow divergence with relevance to blood flow simulations, *Computational Mechanics*, 48(3):277–291, (2011).

[25] Westerhof, N., Lankhaar J.-W., and Westerhof, B.E.: The arterial windkessel, *Medical and Biological Engineering and Computing*, 47(2):131–141, (2009).